Published in final edited form as:
Magn Reson Med. 2014 October ; 72(4): 986–995. doi:10.1002/mrm.25004.

Radial Spectroscopic MRI of Hyperpolarized [1-^{13}C]Pyruvate at 7 T

Marc S. Ramirez[1], **Jaehyuk Lee**[1], **Christopher M. Walker**[1], **Vlad C. Sandulache**[2,3], **Franciszek Hennel**[4], **Stephen Y. Lai**[2], and **James A. Bankson**[1,*]

[1]The Department of Imaging Physics, The University of Texas M.D. Anderson Cancer Center, Houston, TX, USA

[2]The Department of Head and Neck Surgery, The University of Texas M.D. Anderson Cancer Center, Houston, TX, USA

[3]Bobby R. Alford Department of Otolaryngology - Head and Neck Surgery, Baylor College of Medicine, Houston, TX, USA

[4]Bruker BioSpin MRI, Ettlingen, Germany

Abstract

Purpose—The transient and nonrenewable signal from hyperpolarized metabolites requires extensive sequence optimization for encoding spatial, spectral, and dynamic information. In this work, we evaluate the utility of radial single-timepoint and cumulative spectroscopic MRI of hyperpolarized [1-^{13}C] pyruvate and its metabolic products at 7 T.

Methods—Simulations of radial echo planar spectroscopic imaging (EPSI) and multiband frequency encoding (MBFE) acquisitions were performed to confirm feasibility and evaluate performance for HP ^{13}C imaging. Corresponding sequences were implemented on a 7-T small-animal MRI system, tested in phantom, and demonstrated in a murine model of anaplastic thyroid cancer.

Results—MBFE provides excellent spectral separation but is susceptible to blurring and T_2* signal loss inherent to using low readout gradients. The higher readout gradients and more flexible spectral encoding for EPSI result in good spatial resolution and spectral separation. Radial acquisition throughout HP signal evolution offers the flexibility for reconstructing spatial maps of mean metabolite distribution and global dynamic time courses of multiple metabolites.

Conclusion—Radial EPSI and MBFE acquisitions are well-suited for hyperpolarized ^{13}C MRI over short and long durations. Advantages to this approach include robustness to non-stationary magnetization, insensitivity to precise acquisition timing, and versatility for reconstructing dynamically acquired spectroscopic data.

Keywords

Hyperpolarized; ^{13}C; radial; projection; multiband; EPSI; MRSI; anaplastic thyroid cancer

*Please address correspondence to: James A. Bankson, Department of Imaging Physics, Unit 56, The University of Texas M. D. Anderson Cancer Center, 1515 Holcombe Boulevard, Houston, TX 77030-4009, Phone: (713) 792-4273, Fax: (713) 745-9236, jbankson@mdanderson.org.

Introduction

Hyperpolarization technologies (1–3) can temporarily enhance the MR signal of biologically relevant nuclei by several orders of magnitude. This is particularly useful for improved detection of the ^{13}C isotope, which has a low MR sensitivity and low natural abundance. Noninvasive image-based biomarkers of cellular metabolism may be established *in vivo* by monitoring the conversion of hyperpolarized (HP) [1-^{13}C] pyruvate into HP lactate (4,5) because many malignancies maintain remarkably high levels of glycolysis and lactic acid fermentation compared to normal tissue (6,7). There is tremendous potential for the use of HP agents to explore cancer and response to therapy with spatial, temporal, and chemical specificity that was previously not possible.

Unfortunately, HP ^{13}C metabolites are short-lived because magnetization decays according to T_1 relaxation and signal is irreversibly spent with every radiofrequency (RF) excitation. Furthermore, optimal timing of the data sampling window depends on a myriad of biological and experimental factors, including HP agent handling and the kinetics of perfusion and metabolism. It is therefore critical that data acquisition strategies be carefully designed to best utilize the available magnetization over the duration of the experiment, while balancing tradeoffs among spatial, temporal, and spectral resolutions. At one end of the sequence design continuum, dynamic pulse-acquire MRS uses magnetization to read spectral and temporal dynamics with minimal spatial localization provided by slice prescription and coil sensitivity. At the other end, single-shot methods spend magnetization for spatial encoding alone, exploiting the known chemical shift of target metabolites with spatial-spectral excitations that obviate spectral encoding (8). Complex spectroscopic imaging sequences employ 2D and 3D *k*-space trajectories to encode spectral information with multiple spatial dimensions (9,10), often requiring high readout bandwidths or providing low spatial resolution due to limitations in *k*-space coverage in a readout window that is limited by T_2^* relaxation. Sequences that provide reduced acquisition bandwidth and modest spatial encoding per excitation (11–13) are necessary for additional experimental flexibility in the optimization of sensitivity and resolution across multiple field strengths.

Cartesian sampling of *k*-space with conventional phase encoding places severe limitations on spectroscopic imaging (14) and this is exacerbated for imaging time-varying HP metabolites (15). Valuable signal excitations are spent acquiring high spatial frequencies alone, where the detected signal provides a low return on magnetization spent. Alternatively, non-Cartesian sampling, such as with radial (16–18) or spiral (8,9,19–23) trajectories, are desirable for HP imaging since each excitation has a corresponding readout through the center of *k*-space.

The benefits of radial sampling, including robustness to motion artifacts, insensitivity of image contrast to undersampling, and compatibility with dynamic sampling, have led to its use for imaging HP ^{3}He and ^{129}Xe gases (16,24,25). Radial sampling efficiently encodes 2D images with minimal coverage of *k*-space per excitation, allowing for the use of low readout gradients or rapid resampling of *k*-space for spectral discrimination. Radial sampling is also particularly conducive to constrained reconstructions that incorporate prior knowledge (26–

28). In this work, we investigate two radial acquisition methods for visualizing HP [1-^{13}C] pyruvate and its metabolic products over short and long acquisition windows. The first method is a radial version of echo planar spectroscopic imaging (EPSI) (17,29) which involves continuous projection acquisition over several echoes to simultaneously encode spatial and spectral dimensions with high resolution. The second method is a radial adaptation of multiband frequency encoding (MBFE) (13,30), which uses very low readout gradient amplitudes and permits simultaneous spatial and spectral encoding within a single echo per projection.

The utility of radial acquisitions and their corresponding reconstructions were evaluated under conditions that are appropriate for imaging HP [1-^{13}C] pyruvate and its metabolic products in murine models of cancer at 7 T. Numerical simulations helped assess imaging performance and were used to investigate correlation between cumulative reconstructions of radially-sampled HP data and the assumed tracer dynamics. Radial EPSI and MBFE pulse sequences were implemented and tested using imaging phantoms containing enriched urea and alanine at thermal equilibrium. Finally, *in vivo* images of mice bearing anaplastic thyroid tumors were acquired using the two approaches, demonstrating the utility of radial sampling for HP ^{13}C imaging.

Methods

Three 2D radial imaging protocols were evaluated in simulation and through measurements in phantom and *in vivo* on a BioSpec 7-T/30-cm small animal imaging system (Bruker Biospin MRI, Inc., Ettlingen, Germany): one based on EPSI, and two variations of MBFE. All sequences were prescribed for a 3-cm FOV over a 1-cm slice thickness. Projection angles were incremented by 111° to balance orthogonality among projections that are acquired nearby in time (18,31). For convenience, basic pulse sequence diagrams are shown in Figure 1 and acquisition parameters for the protocols are summarized in Table 1. Major differences between EPSI and MBFE are described in the following sections.

Echo Planar Spectroscopic Imaging

EPSI uses an alternating readout gradient to simultaneously encode both spatial and spectral information during data acquisition (12,15,29,32,33). The signal measured from a projection of a radially-encoded object containing multiple metabolites with chemical shifts δ_m with respect to a convenient reference in the center of the spectral window, can be written as:

$$s(k_r,t)=\sum_{m=1}^{N_{metabs}} \int \rho_m(r) e^{\frac{-t}{T_2^*}} e^{i2\pi f_o \delta_m t_e - i2\pi k_r(t)\cdot r} d_r, \quad [1]$$

where r represents the spatial dimension for the radial projection, ρ_m is the density of the m^{th} metabolite, and $k_r(t)$ is the periodic echo-planar radial k-space trajectory with period T = 2ΔTE (Figure 2). After correction for spin evolution within and between echoes (34), Fourier transformation provides artifact-free spectral information with a bandwidth equal to 1/(2ΔTE) for each point along readout. As shown in Figure 2, maps of frequency vs. radial

offset can be calculated from the echo train acquired for each projection angle. Integration over the spectral width of peaks corresponding to individual metabolites yields projection data that can be used to reconstruct spectrally resolved images.

The technical challenges inherent to EPSI with HP [1-^{13}C] pyruvate vary with field strength. Larger frequency differences between metabolites require a higher spectral bandwidth and thus lower echo spacing to control spectral aliasing. This is particularly burdensome when data from several metabolites is spectrally undersampled, and aliasing may cause overlap among peaks. Here, a bipolar gradient approach was implemented to achieve the lowest ΔTE spacing for a given spatial resolution and readout bandwidth (15). Echo spacing that minimized spectral contamination due to undersampling and N/2 ghosting was chosen based on data from a previous *in vivo* study (35).

Multiband Frequency Encoding

An alternative to traditional spectroscopic imaging methods was recently introduced (13). MBFE allows simultaneous separation of spatial and spectral components in one echo per projection without rapidly switching gradients. This approach requires that the readout gradient G_{RO} is reduced to ensure that the frequency encoding bandwidth across the image field of view (FOV) is less than the minimum chemical shift between metabolites, $\Delta\delta_{min}$ (13):

$$G_{RO} \leq \frac{\Delta\delta_{min} B_o}{FOV}. \quad [2]$$

The readout bandwidth BW_{RO} is decoupled from the readout gradient strength and increased along with the number of readout points to accommodate the frequency encoding bandwidth around all expected chemical species. Assuming equality in Eq. [2], the number of distinct frequency encoding bands can be determined by $\Delta\delta_{min}$ and the largest chemical shift among metabolites, $\Delta\delta_{max}$ (Figure 3):

$$N_{Bands} = \frac{\Delta\delta_{max} + \Delta\delta_{min}}{\Delta\delta_{min}}. \quad [3]$$

The FOV for each metabolite is encoded over offset frequency encoding bandwidths, as illustrated in Figure 2:

$$BW_{RO/Band} = \Delta\delta_{min} B_0 \gamma_{13C}, \quad [4]$$

$$N_{Ro/Band} = \frac{FOV}{Res}, \quad [5]$$

and the overall readout bandwidth and matrix size are given by the products of Eq. [3] with Eqs. [4] and [5]. Here, *Res* indicates the target spatial resolution along the readout gradient, which is primarily limited by SNR and T_2* decay. Low readout bandwidths, corresponding with low $\Delta\delta_{max}$ and $\Delta\delta_{min}$, result in long dwell times for data acquisition, which lead to an increase in the minimum achievable echo time, lower SNR, and reduced intrinsic spatial

resolution due to blurring. Low readout gradients may also lead to spatial distortions in the presence of B_0 inhomogeneities (13).

Because the performance of MBFE is highly dependent on $\Delta\delta_{min}$, we considered two imaging scenarios: *A*) where four metabolites (pyruvate, lactate, alanine, and pyruvate-hydrate) are present and have sufficient signal and are of sufficient interest to be measured, and *B*) where alanine and pyruvate-hydrate signals are below the acquisition noise floor, have been suppressed (36), or can otherwise be discarded. To accommodate all metabolites, a readout bandwidth consisting of almost six frequency encoding bands (Eq. [3]) was used for scenario *A*, whereas two bands were used for scenario *B*.

Numerical Phantom Simulations: Single-Timepoint

To investigate the feasibility of the imaging strategies and to test image reconstructions, simulations were performed in Matlab (MathWorks, Natick, MA, USA). Numerical phantoms consisting of cylindrical compartments (6.6-mm outer diameter) of pyruvate, lactate, alanine, pyruvate-hydrate, and both pyruvate and lactate were created within a 3-cm FOV. Time samples from each compartment were calculated using radial *k*-space trajectories (37) modulated by their relative chemical shifts and transverse relaxation according to Eq. [1]. Signals from all compartments were summed to synthesize raw data. Based on previous *in vivo* acquisitions at 7 T, signal decay according to an apparent T_2^* = 12 ms was included. A variable flip angle excitation scheme (38) was assumed to generate equal transverse magnetization for every projection. T_1 decay was neglected because we first consider the use of these sequences for rapid data acquisition over a short interval of time. We have previously measured the T_1 relaxation time of *ex vivo* HP [1-^{13}C] pyruvate at 7 T to be 62.8 s ± 0.8 s.

For MBFE, synthetic raw data were Fourier transformed along the readout direction and a filtered backprojection algorithm was then applied to each frequency encoding band to generate the metabolite images. Bipolar EPSI data were corrected (34), transformed, and integrated over the full width at half maximum of spectral peaks to generate metabolite-specific projections. Images were generated by simple backprojection of the filtered data.

To estimate SNR performance of the imaging sequences developed in this work, simulations were repeated on a homogeneous numerical phantom. All conditions for the numerical experiment were assumed constant except for those affected by acquisition parameters. Gaussian noise with a standard deviation proportional to the square root of the receiver bandwidth ($\sqrt{BW_{RO}}$) was added to the synthetic *k*-space samples $s(k_r,t)$. The addition of noise in the raw domain ensures that its effects correctly propagate through all subsequent steps in processing and analysis. To avoid SNR dependence on the image reconstruction algorithm or the number of acquired projections, relative signal and noise were estimated from the mean and standard deviation respectively, from the center of a common projection.

Numerical Phantom Simulations: Tracer Averaging

In contrast to HP imaging with variable flip angle excitations, projections resulting from constant flip angles over a longer interval of time are weighted by HP metabolite dynamics

and activity. This is useful for dynamic imaging, where data may be used to derive kinetic information. We hypothesized that direct filtered backprojection of constant flip angle data, acquired over the entire course of the observable HP signal, could provide a semi-quantitative estimate of metabolite distribution. To investigate, a numerical phantom simulation was performed in which dynamic HP metabolite curves were generated to correspond with regions of normal and tumor tissues. Evolution of metabolite dynamics was estimated by kinetic modeling based on prior data (39,40). Up to 3-second variations in the HP agent arrival time, 200% variations in signal amplitude, and 40% variations in enzyme concentration were applied to increase phantom heterogeneity. Projections of the dynamic numerical phantom were generated every 1 s, with 111° projection angle increments, and assuming a 10° excitation angle. Noise corresponding with a peak lactate SNR of six in normal tissue was added.

A clear advantage in the use of simulations to investigate and compare acquisition strategies lies in our ability to know and control the truth against which our observations are compared. This is particularly beneficial in the investigation of sequences for HP imaging, where excitations deplete the signal available from both the substrate and its downstream metabolites and may bias observations. To investigate the accuracy and potential bias of this approach, we compared the cumulative filtered backprojected images to the temporal mean of the known signals both with and without the influence of signal excitation.

Phantom Imaging

Radial MBFE and EPSI sequences were created by modifying a conventional multislice gradient echo pulse sequence. Compared to MBFE, which requires a single echo to perform spectroscopic imaging, the gradient trajectory required for radial EPSI is potentially susceptible to *k*-space sampling errors. To investigate the gradient performance of our system for HP spectroscopic imaging with the EPSI protocol described in Table 1, *k*-space trajectories were measured on a homogeneous 8-M urea phantom using a well-established method (41). Signal averaging was required to enhance SNR so that trajectories at late echo times could be evaluated. To reduce overall acquisition time, eight projection angles were evaluated with 22.5° increments.

To evaluate the sequence performance for spectroscopic imaging, a multi-compartment phantom containing 8-M urea (~165 ppm) and 3-M acetate (~183 ppm) was assembled and placed within a 7-T small animal imaging system equipped with a single channel for carbon reception and gradients with a 12-cm inner diameter (ID), a 200-mT/m maximum strength, and 80-μs ramp time. A standard dual-tuned $^{1}H/^{13}C$ volume coil (72-mm ID, Bruker Biospin MRI, Inc., Ettlingen, Germany) was used for transmit and receive. Sequences were modified slightly to accommodate the higher spectral separation (~18 ppm) between these substances. Both acquisitions covered a 3-cm FOV over 32 readout points, 300 projections, 20 averages, 1-cm slice thickness, and 40° flip angle. The MBFE sequence used a TE/TR = 10.5/300 ms, 30% echo position, and BW_{read} = 2.8 kHz. The EPSI sequence used TE_1/TR = 2.0/300 ms, ΔTE = 1.22 ms, $BW_{spectral}$ = 819 Hz, and BW_{read} = 34.7 kHz. Data were acquired at thermal equilibrium and images were reconstructed by filtered backprojection.

In Vivo Acquisitions

Male nude mice bearing orthotopic xenografts of anaplastic thyroid cancer (42) were used to demonstrate *in vivo* acquisitions. Prior to imaging, the animals were anesthetized, catheterized via tail vein, and placed supine on a mouse sled distributing 2% isoflurane in oxygen through nose cones. Respiratory rates and body temperature were monitored with a commercial small-animal monitoring system (Small Animal Instruments, Inc., Stony Brook, New York). A custom-built two-turn ^{13}C surface coil (1.5-cm ID) was placed over the tumors for improved sensitivity.

Using a HyperSense (Oxford Instruments, Abingdon, Oxfordshire, UK) dynamic nuclear polarization (DNP) polarizer, a 20-μL aliquot of [1-^{13}C] neat pyruvic acid with 15 mM of the trityl radical OX063 (GE Healthcare, Waukesha, WI, USA) and 1.5-mM Prohance was polarized at 1.4 K and 3.35 T using 94.2-GHz microwave irradiation for 40 minutes. The frozen sample was then dissolved at 180°C in a 4-mL buffer containing 40-mM TRIS, 80-mM NaOH, and 50-mM NaCl to a final isotonic and neutral solution containing 80-mM HP [1-^{13}C] pyruvate. After dissolution, 200 μL were administered to animals via tail-vein catheter over a 12-s duration. All animal procedures were approved by our Institutional Animal Care and Use Committee, which is accredited by the Association for the Assessment and Accreditation of Laboratory Animal Care International.

The radial sequences were demonstrated on animals with early- and late-stage tumors. ^{1}H scout images, to confirm animal position and tumor location, were followed by coronal and axial T_2-weighted anatomical acquisitions (TE/TR = 17/2500 ms, 3.0-cm FOV, 256 × 256 matrix, 9 1.5-mm slices, 5 averages, RARE factor = 8). A 1-cm axial slice was prescribed over the tumor for the ^{13}C acquisition. A 0.69-ms, 4-kHz bandwidth Gauss pulse was used for excitation. The center frequency was set between resonances of [1-^{13}C] pyruvate and [1-^{13}C] lactate, resulting in 1.2-mm offsets (in opposing directions) between the prescribed slice location and the actual pyruvate and lactate slices, which was minor compared to the slice thickness. Because alanine and pyruvate-hydrate were not detected in a preliminary MBFE mouse acquisition representing scenario *A*, sequence parameters corresponding with scenario *B* were used for final *in vivo* demonstration. The variable flip angle MBFE sequence was initiated 25 seconds after the commencement of injection, where lactate signal was expected to be highest. With 50 projections and a 60-ms TR, the total acquisition time was 3 seconds. Pyruvate and lactate frequencies were confirmed from a slice-localized pulse-acquire readout by setting readout gradient levels to zero during the final projection acquisition. The EPSI sequence was initiated prior to the HP agent injection and 200 projections were acquired at 1-s intervals. In addition to the cumulative filtered backprojection reconstruction, total signal from HP pyruvate and lactate were calculated by integrating along the radial dimension of each projection to form a global estimate of signal dynamics.

Results

For the EPSI sequence, a 9.9-ppm spectral bandwidth is achieved with $\Delta TE = 1.35$ ms. With this echo spacing, lactate aliases into the acquisition band but does not overlap with other

metabolites (Figure 3). Furthermore, any spectral N/2 ghosts of lactate do not interfere with the pyruvate signal or vice versa.

The feasibility of these strategies was confirmed by simulation as shown in Figure 4. All metabolites are spectrally distinguished with EPSI and MBFE version *A*, in which $\Delta\delta_{min}$ is established by the 2.6-ppm chemical shift between alanine and pyruvate hydrate (Figure 3). For MBFE version *B*, in which only pyruvate and lactate are measured, $\Delta\delta_{min} = \Delta\delta_{max} =$ 12.2 ppm and two frequency encoding bands are sufficient for encoding with much higher intrinsic spatial resolution (full width at half maximum = 0.86 mm, compared to 4.06 mm for MBFE version *A*).

Although SNR depends on the sequence parameters selected for a particular application and field strength, numerical simulations provide general insight regarding SNR for murine imaging at 7 T. Both gradient echo MBFE and EPSI strategies suffer signal loss due to T_2* decay. Unlike EPSI, where the initial echo time is well below T_2*, the long MBFE readout window leads to echo times beyond the apparent T_2*, compromising SNR. Comparing sequences with identically prescribed spatial resolutions, EPSI provided an SNR that was approximately 26% higher than that observed from MBFE version *B*. MBFE version A provided 2× higher SNR compared to MBFE version *B*, but at much lower spatial resolution.

Metabolite images from backprojected data that are sampled throughout the HP signal time-courses correlate well with the true mean metabolite signal over time (Figure 5). As expected, cumulative images of pyruvate and lactate correlate best ($R^2 = 0.92$) with the temporal average of signals affected by RF excitations. A high correlation ($R^2 = 0.89$) with mean polarization ignoring the effects of RF excitations suggests minimal bias in the estimation of *in vivo* dynamics. This demonstrates a clear benefit for radial sampling of HP agents, since the center of *k*-space is sampled following each excitation. Radial spectroscopic imaging over the whole duration of the polarized agent is insensitive to the precise timing requirements that are necessary for reproducible single-timepoint images, since the ratio of metabolite concentrations changes continuously in time.

Representative trajectories from the radial EPSI sequence are shown in Figure 6. As expected, sampling at early echo times results in minimal deviation from the ideal case: maximum deviation for the first echo is less than 0.04 times Δk, the radial *k*-space sampling resolution. Late in the echo train, where the measurement becomes more significantly affected by noise and T_2* signal attenuation, the minimum distance from the origin never exceeded approximately Δk/3.

The phantom images of Figure 7 confirm the successful implementation of radial MBFE and EPSI pulse sequences and demonstrate spectral separation of ^{13}C-labeled substrates with both approaches. Finally, *in vivo* images of mice bearing anaplastic thyroid tumors are shown in Figure 8. Metabolite maps were overlaid on T_2-weighted images to demonstrate correlation with anatomy. For both imaging methods, lactate levels are elevated in the tumor compared to surrounding tissue. Highest levels of pyruvate are proximal to major vessels, and pyruvate is more prominent in the cumulative acquisition compared to the single-

timepoint acquisition. *In vivo* measurement of B_0 homogeneity with the surface coil in place revealed a root-mean-square offset of 0.15 ppm, suggesting modest blurring in images acquired from MBFE scenario *B* that would be impractically high in scenario *A*. These offsets have negligible impact on EPSI because of comparatively high readout bandwidth and integration over an encompassing spectral range to form metabolite-specific projection data. Metabolite time courses derived from the EPSI data (Figure 8) demonstrate the utility and flexibility for cumulative radial sampling throughout the signal lifetime. Data can be reconstructed to derive maps of mean HP metabolites over time with good spatial resolution, and alternatively, spatial information may be sacrificed to generate dynamic time courses localized by the coil sensitivity and by slice selection.

Discussion

We have successfully demonstrated the use of two radial acquisition methods for spectroscopic imaging of HP [1-^{13}C] pyruvate and its metabolic products at 7 T. Feasibility was confirmed through numerical simulation and experimental observations in phantom and *in vivo*. Simulations revealed the relative data resolution and SNR performance of radial gradient-echo implementations of EPSI and MBFE. Each approach has advantages and shortcomings that might make it the method of choice under specific experimental circumstances.

EPSI is desirable for spectroscopic imaging because of its flexibility. Spectral undersampling can be used to limit readout bandwidth and improve SNR, to increase spatial resolution, or both. In this work, bipolar echo planar gradients were used to minimize echo spacing for a given spatial resolution and readout bandwidth. Care was taken to reproducibly suppress confounding N/2 ghosting among metabolites (34). EPSI is also potentially susceptible to *k*-space trajectory inaccuracies due to non-ideal gradient waveforms, potentially affecting both image quality and spectral resolution. Radial EPSI trajectory measurements performed on a homogenous phantom indicated minimal error that is not expected to significantly compromise spectroscopic imaging performance. More significant deviation from ideal *k*-space trajectory can be assessed and corrected through calibration scans.

Radial spectroscopic imaging with MBFE performs well when a limited number of metabolites with large minimum spectral separations (i.e. $\Delta\delta_{min}$) are detected. For HP imaging of [1-^{13}C] pyruvate, multiband excitation pulses (36) could be used to suppress the alanine and pyruvate-hydrate signals (13), but would further increase attainable gradient echo times due to long pulse durations that would further exaggerate degradations due to T_2* decay. Spectral spatial pulses for HP ^{13}C imaging have primarily been limited to spin echo acquisitions with adiabatic refocusing pulses (10). Simulations demonstrate that SNR for gradient echo EPSI is generally higher than a gradient echo MBFE acquisition with similar spatial resolution. EPSI uses higher readout bandwidths, which leads to better intrinsic spatial resolution, and the earlier initial echo time significantly reduces signal loss due to T_2* decay. Pilot simulations indicate that spin-echo adaptations of these sequences would minimize this effect, but a thorough investigation of their practical limitations is beyond the scope of this manuscript.

Although hyperpolarization offers dramatic increases in signal for key substrates and their downstream metabolites, gain is transient and nonrenewable, and encoding strategies must be carefully optimized to achieve measurements with clinically relevant spatial, spectral, and temporal resolutions. All available tools must be included to maximize accuracy and reproducibility. In this study, a surface coil was placed directly over the region of interest to improve detection. A drawback associated with this strategy is signal dependence on coil placement and heterogeneous weighting of images due to the coil sensitivity. In this work, pyruvate signal near coil conductors appeared slightly elevated in the constant flip angle EPSI image (Figure 8). Future development of ^{13}C RF detectors, including coil arrays, will be required to overcome current limitations and further sequence optimization remains.

All sequences in this work were optimized for murine imaging at 7 T; however the results can be used to gain insight at other field strengths. For lower B_0, the frequency range associated with $\Delta\delta_{min}$ and $\Delta\delta_{max}$ are reduced, leading to lower minimum BW_{RO} and higher dwell times for MBFE. This in combination with a fixed N_{RO}, would lead to higher signal loss due to transverse relaxation. For EPSI at low fields, the spectral aliasing described in this work could be maintained with longer ΔTE spacing, permitting lower readout bandwidths and potentially leading to higher SNR. Due to transverse relaxation however, increasing echo spacing would also reduce the number of acquired echoes that maintain detectable signal, potentially limiting spectral resolution. At higher fields, the constraints associated with MBFE become more attractive.

More exotic spatial encoding trajectories (17,43,44) may be employed, but not without some sacrifice in EPSI echo spacing and thus spectral resolution. EPSI sequences at high field strength, such as 7 T, already tax the acquisition hardware and require spectral aliasing to reduce bandwidth and maintain SNR. Undersampling strategies such as those employed with compressed sensing (45) may also be incorporated into future acquisitions (10,46).

The radial sequences developed in this work can be used for rapid, single-timepoint observations, or cumulative observations that are distributed in time over the observable HP lifetime. The speed of data acquisition is not limited by traditional signal recovery due to longitudinal relaxation, but rather by the evolution of interactions between the HP substrate and target biology. Snapshot spectroscopic imaging with MBFE over a 3-s acquisition window was demonstrated in this work. Because the specific distribution of tracers in this window of time depends on metabolic activity as well as multiple upstream variables such as tracer handling and tumor perfusion, the reproducibility of this approach may be limited. Alternatively, continuous radial acquisition over the whole HP lifetime, as simulated in this work and demonstrated *in vivo*, results in images that correlate well with the mean polarization of metabolites over time and provides a method for deriving global dynamic time courses. Data acquired using other trajectories such as spiral may also be used to generate estimates of average signal intensity, as long as the approach to reconstruction does not require global self-consistency that is not strictly supported. Filtered backprojection reconstruction was used in this work to avoid artifacts due to dramatic changes in the distribution of magnetization over the course of tracer lifetime. Much work remains in determining optimal acquisition strategies for the most robust measure of changes in cancer

metabolism through image-based biomarkers, but preliminary results for radial acquisitions are encouraging.

In conclusion, we have established the utility of radial acquisitions for imaging HP [1-^{13}C] pyruvate and its metabolic products, for single-timepoint and cumulative acquisitions at 7 T. Radial EPSI and MBFE are both viable options for spectroscopic MRI of HP ^{13}C metabolites. Advantages of radial HP MRI include robustness to spin motion and insensitivity to precise acquisition timing, where a semi-quantitative estimate of mean polarization over time can be directly generated. Radial acquisitions are well-suited for HP ^{13}C MRI and illustrate an attractive acquisition strategy for *in vivo* imaging with HP agents.

Acknowledgments

We thank Marcus Monroe, Yun Yun Chen, Charles Kingsley, Kiersten Maldonado, and Jorge de la Cerda for their support in preparing the animals. This work was supported in part by the National Institutes of Health (P30-CA016672) and the Cancer Prevention and Research Institute of Texas (RO-101243-P5). Funding as an Odyssey Fellow was supported by the Odyssey Program and The Estate of C.G. Johnson, Jr. at The University of Texas M.D. Anderson Cancer Center.

References

1. Bowers CR, Weitekamp D. Parahydrogen and synthesis allow dramatically enhanced nuclear alignment. Journal of the American Chemical Society. 1987; 109(18):5541–5542.
2. Middleton H, Black RD, Saam B, Cates GD, Cofer GP, Guenther R, Happer W, Hedlund LW, Johnson GA, Juvan K, et al. MR imaging with hyperpolarized 3He gas. Magn Reson Med. 1995; 33(2):271–275. [PubMed: 7707920]
3. Ardenkjaer-Larsen JH, Fridlund B, Gram A, Hansson G, Hansson L, Lerche MH, Servin R, Thaning M, Golman K. Increase in signal-to-noise ratio of >10,000 times in liquid-state NMR. Proc Natl Acad Sci U S A. 2003; 100(18):10158–10163. [PubMed: 12930897]
4. Albers MJ, Bok R, Chen AP, Cunningham CH, Zierhut ML, Zhang VY, Kohler SJ, Tropp J, Hurd RE, Yen YF, Nelson SJ, Vigneron DB, Kurhanewicz J. Hyperpolarized 13C lactate, pyruvate, and alanine: noninvasive biomarkers for prostate cancer detection and grading. Cancer Res. 2008; 68(20):8607–8615. [PubMed: 18922937]
5. Golman K, Olsson LE, Axelsson O, Mansson S, Karlsson M, Petersson JS. Molecular imaging using hyperpolarized 13C. Br J Radiol. 2003; 76(Spec No 2):S118–S127. [PubMed: 15572334]
6. Warburg O. On the origin of cancer cells. Science. 1956; 123(3191):309–314. [PubMed: 13298683]
7. Feron O. Pyruvate into lactate and back: from the Warburg effect to symbiotic energy fuel exchange in cancer cells. Radiother Oncol. 2009; 92(3):329–333. [PubMed: 19604589]
8. Lau AZ, Chen AP, Ghugre NR, Ramanan V, Lam WW, Connelly KA, Wright GA, Cunningham CH. Rapid multislice imaging of hyperpolarized 13C pyruvate and bicarbonate in the heart. Magn Reson Med. 2010; 64(5):1323–1331. [PubMed: 20574989]
9. Mayer D, Yen YF, Tropp J, Pfefferbaum A, Hurd RE, Spielman DM. Application of subsecond spiral chemical shift imaging to real-time multislice metabolic imaging of the rat in vivo after injection of hyperpolarized 13C1-pyruvate. Magn Reson Med. 2009; 62(3):557–564. [PubMed: 19585607]
10. Larson PE, Hu S, Lustig M, Kerr AB, Nelson SJ, Kurhanewicz J, Pauly JM, Vigneron DB. Fast dynamic 3D MR spectroscopic imaging with compressed sensing and multiband excitation pulses for hyperpolarized 13C studies. Magn Reson Med. 2011; 65(3):610–619. [PubMed: 20939089]
11. Larson PE, Bok R, Kerr AB, Lustig M, Hu S, Chen AP, Nelson SJ, Pauly JM, Kurhanewicz J, Vigneron DB. Investigation of tumor hyperpolarized [1-13C]-pyruvate dynamics using time-resolved multiband RF excitation echo-planar MRSI. Magn Reson Med. 2010; 63(3):582–591. [PubMed: 20187172]

12. Cunningham CH, Chen AP, Albers MJ, Kurhanewicz J, Hurd RE, Yen YF, Pauly JM, Nelson SJ, Vigneron DB. Double spin-echo sequence for rapid spectroscopic imaging of hyperpolarized 13C. J Magn Reson. 2007; 187(2):357–362. [PubMed: 17562376]
13. von Morze C, Reed G, Shin P, Larson PE, Hu S, Bok R, Vigneron DB. Multi-band frequency encoding method for metabolic imaging with hyperpolarized [1-(13)C]pyruvate. J Magn Reson. 2011; 211(2):109–113. [PubMed: 21596601]
14. Adalsteinsson E, Irarrazabal P, Topp S, Meyer C, Macovski A, Spielman DM. Volumetric spectroscopic imaging with spiral-based k-space trajectories. Magn Reson Med. 1998; 39(6):889–898. [PubMed: 9621912]
15. Yen YF, Kohler SJ, Chen AP, Tropp J, Bok R, Wolber J, Albers MJ, Gram KA, Zierhut ML, Park I, Zhang V, Hu S, Nelson SJ, Vigneron DB, Kurhanewicz J, Dirven HA, Hurd RE. Imaging considerations for in vivo 13C metabolic mapping using hyperpolarized 13C-pyruvate. Magn Reson Med. 2009; 62(1):1–10. [PubMed: 19319902]
16. Wild JM, Paley MN, Kasuboski L, Swift A, Fichele S, Woodhouse N, Griffiths PD, van Beek EJ. Dynamic radial projection MRI of inhaled hyperpolarized 3He gas. Magn Reson Med. 2003; 49(6):991–997. [PubMed: 12768575]
17. Wang, K.; Peterson, E.; Gordon, J.; Kurpad, K.; Rowland, I.; Erickson, M.; Fain, S. Dynamic Hyperpolarized C-13 Spectroscopic Imaging using Radial Acquisition and HYPR Reconstruction; Proceedings of the 18th Annual Meeting of ISMRM; Montreal, Quebec, Canada. 2010. p. 3267
18. Laustsen, C.; Ringgard, S.; Birn, H.; Pedersen, M.; Ardnekjaef-Larsen, JH. Radial Golden Angle Fast Spin Echo: A Hyperpolarized 13C Multi Contrast Method; Proceedings of the 21st Annual Meeting of ISMRM; Salt Lake City, Utah, USA. 2013. p. 1928
19. Kim DH, Adalsteinsson E, Spielman DM. Spiral readout gradients for the reduction of motion artifacts in chemical shift imaging. Magn Reson Med. 2004; 51(3):458–463. [PubMed: 15004785]
20. Wiesinger F, Weidl E, Menzel MI, Janich MA, Khegai O, Glaser SJ, Haase A, Schwaiger M, Schulte RF. IDEAL spiral CSI for dynamic metabolic MR imaging of hyperpolarized [1-13C]pyruvate. Magn Reson Med. 2012; 68(1):8–16. [PubMed: 22127962]
21. Schulte RF, Sperl JI, Weidl E, Menzel MI, Janich MA, Khegai O, Durst M, Ardenkjaer-Larsen JH, Glaser SJ, Haase A, Schwaiger M, Wiesinger F. Saturation-recovery metabolic-exchange rate imaging with hyperpolarized [1-13C] pyruvate using spectral-spatial excitation. Magn Reson Med. 2013; 69(5):1209–1216. [PubMed: 22648928]
22. Gordon, J.; Fain, SB.; Johnson, K. Direct Estimation of Hyperpolarized Metabolites with IDEAL Spiral CSI; Proceedings of the 20th Annual Meeting of ISMRM; Melbourne, Australia. 2012. p. 4299
23. Gordon JW, Niles DJ, Fain SB, Johnson KM. Joint spatial-spectral reconstruction and k-t spirals for accelerated 2D spatial/1D spectral imaging of 13C dynamics. Magn Reson Med. 2013
24. Koumellis P, van Beek EJ, Woodhouse N, Fichele S, Swift AJ, Paley MN, Hill C, Taylor CJ, Wild JM. Quantitative analysis of regional airways obstruction using dynamic hyperpolarized 3He MRI-preliminary results in children with cystic fibrosis. J Magn Reson Imaging. 2005; 22(3):420–426. [PubMed: 16104046]
25. Holmes JH, O'Halloran RL, Brodsky EK, Jung Y, Block WF, Fain SB. 3D hyperpolarized He-3 MRI of ventilation using a multi-echo projection acquisition. Magn Reson Med. 2008; 59(5): 1062–1071. [PubMed: 18429034]
26. Mistretta CA, Wieben O, Velikina J, Block W, Perry J, Wu Y, Johnson K. Highly constrained backprojection for time-resolved MRI. Magn Reson Med. 2006; 55(1):30–40. [PubMed: 16342275]
27. Block KT, Uecker M, Frahm J. Undersampled radial MRI with multiple coils. Iterative image reconstruction using a total variation constraint. Magn Reson Med. 2007; 57(6):1086–1098. [PubMed: 17534903]
28. Ragan DK, Lai SY, Bankson JA. Fast, reproducible measurement of the vascular input function in mice using constrained reconstruction and cardiac sampling. NMR Biomed. 2011; 24(4):373–384. [PubMed: 20862661]
29. Mansfield P. Spatial mapping of the chemical shift in NMR. Magn Reson Med. 1984; 1(3):370–386. [PubMed: 6571566]

30. Reed GD, Larson PE, Morze C, Bok R, Lustig M, Kerr AB, Pauly JM, Kurhanewicz J, Vigneron DB. A method for simultaneous echo planar imaging of hyperpolarized (1)(3)C pyruvate and (1)(3)C lactate. Journal of magnetic resonance. 2012; 217:41–47. [PubMed: 22405760]
31. Winkelmann S, Schaeffter T, Koehler T, Eggers H, Doessel O. An optimal radial profile order based on the Golden Ratio for time-resolved MRI. IEEE Trans Med Imaging. 2007; 26(1):68–76. [PubMed: 17243585]
32. Posse S, Tedeschi G, Risinger R, Ogg R, Le Bihan D. High speed 1H spectroscopic imaging in human brain by echo planar spatial-spectral encoding. Magn Reson Med. 1995; 33(1):34–40. [PubMed: 7891533]
33. Cunningham CH, Vigneron DB, Chen AP, Xu D, Nelson SJ, Hurd RE, Kelley DA, Pauly JM. Design of flyback echo-planar readout gradients for magnetic resonance spectroscopic imaging. Magn Reson Med. 2005; 54(5):1286–1289. [PubMed: 16187273]
34. Hanson LG, Schaumburg K, Paulson OB. Reconstruction strategy for echo planar spectroscopy and its application to partially undersampled imaging. Magn Reson Med. 2000; 44(3):412–417. [PubMed: 10975893]
35. Sandulache VC, Skinner HD, Wang Y, Chen Y, Dodge CT, Ow TJ, Bankson JA, Myers JN, Lai SY. Glycolytic inhibition alters anaplastic thyroid carcinoma tumor metabolism and improves response to conventional chemotherapy and radiation. Mol Cancer Ther. 2012; 11(6):1373–1380. [PubMed: 22572813]
36. Larson PE, Kerr AB, Chen AP, Lustig MS, Zierhut ML, Hu S, Cunningham CH, Pauly JM, Kurhanewicz J, Vigneron DB. Multiband excitation pulses for hyperpolarized 13C dynamic chemical-shift imaging. J Magn Reson. 2008; 194(1):121–127. [PubMed: 18619875]
37. Van de Walle R, Barrett HH, Myers KJ, Altbach MI, Desplanques B, Gmitro AF, Cornelis J, Lemahieu I. Reconstruction of MR images from data acquired on a general nonregular grid by pseudoinverse calculation. IEEE Trans Med Imaging. 2000; 19(12):1160–1167. [PubMed: 11212364]
38. Zhao L, Mulkern R, Tseng CH, Williamson D, Patz S, Kraft R, Walsworth RL, Jolesz FA, Albert MS. Gradient-Echo Imaging Considerations for Hyperpolarized 129Xe MR. J Magn Reson B. 1996; 113(2):179–183.
39. Witney TH, Kettunen MI, Brindle KM. Kinetic modeling of hyperpolarized 13C label exchange between pyruvate and lactate in tumor cells. J Biol Chem. 2011; 286(28):24572–24580. [PubMed: 21596745]
40. Walker CM, Lee J, Ramirez MS, Schellingerhout D, Millward S, Bankson JA. A Catalyzing Phantom for Reproducible Dynamic Conversion of Hyperpolarized [1-13C]-Pyruvate. PLoS One. 8(8):e71274. [PubMed: 23977006]
41. Zhang Y, Hetherington HP, Stokely EM, Mason GF, Twieg DB. A novel k-space trajectory measurement technique. Magn Reson Med. 1998; 39(6):999–1004. [PubMed: 9621924]
42. Nucera C, Nehs MA, Mekel M, Zhang X, Hodin R, Lawler J, Nose V, Parangi S. A novel orthotopic mouse model of human anaplastic thyroid carcinoma. Thyroid. 2009; 19(10):1077–1084. [PubMed: 19772429]
43. Bucholz EK, Song J, Johnson GA, Hancu I. Multispectral imaging with three-dimensional rosette trajectories. Magn Reson Med. 2008; 59(3):581–589. [PubMed: 18306410]
44. Schulte, RF.; Wiesinger, F.; Fish, KM.; Whitt, D.; Hancu, I. Efficient Hyperpolarized 13C Metabolic Imaging with Rosette Spectroscopic Imaging; Proceedings of the 17th Annual Meeting of ISMRM; Honolulu, Hawaii, USA. 2009. p. 2433
45. Lustig M, Donoho D, Pauly JM. Sparse MRI: The application of compressed sensing for rapid MR imaging. Magn Reson Med. 2007; 58(6):1182–1195. [PubMed: 17969013]
46. Hu S, Lustig M, Chen AP, Crane J, Kerr A, Kelley DA, Hurd R, Kurhanewicz J, Nelson SJ, Pauly JM, Vigneron DB. Compressed sensing for resolution enhancement of hyperpolarized 13C flyback 3D-MRSI. J Magn Reson. 2008; 192(2):258–264. [PubMed: 18367420]

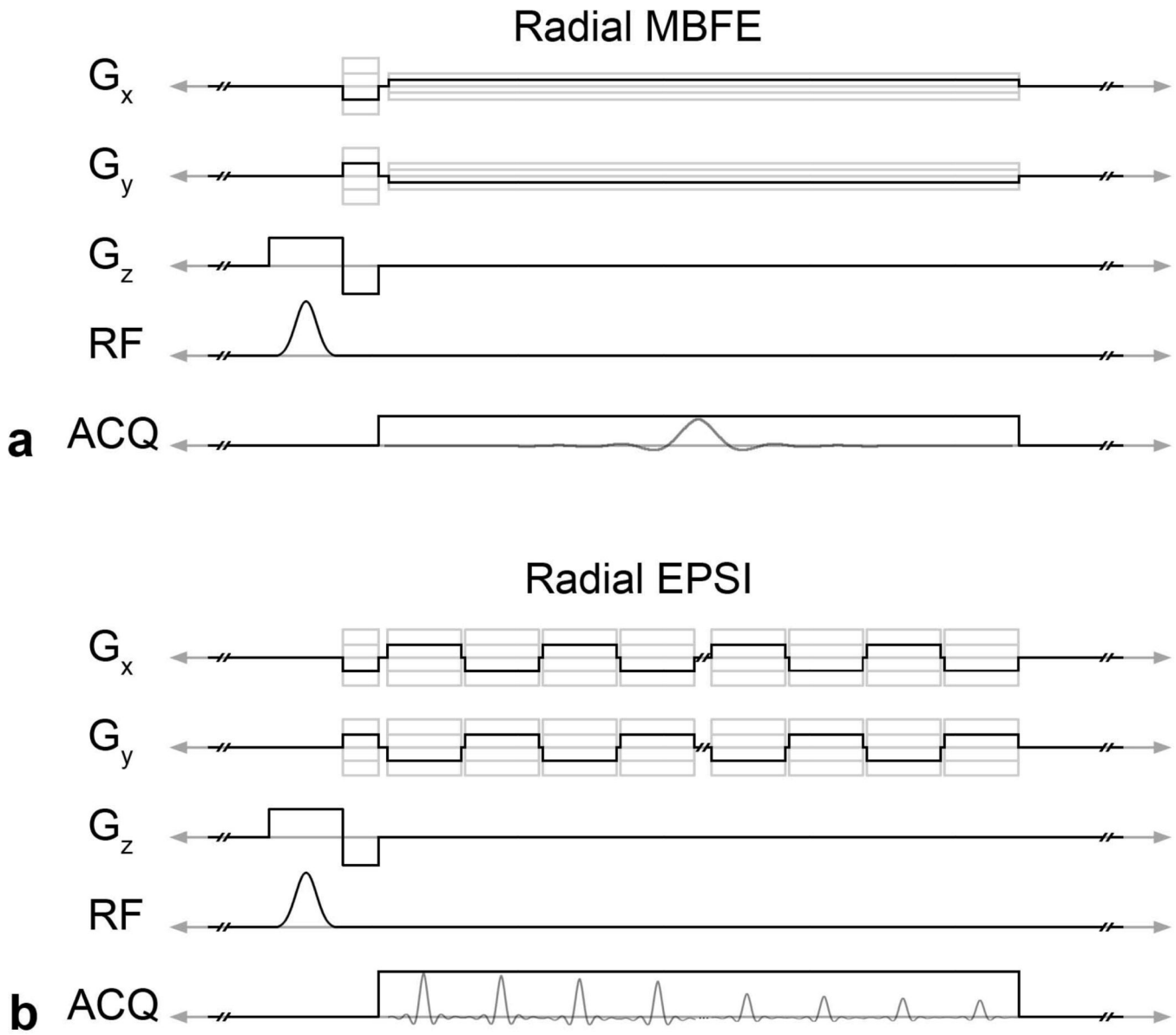

Figure 1.
Pulse sequence diagram for the 2D radial a. MBFE and b. EPSI acquisitions.

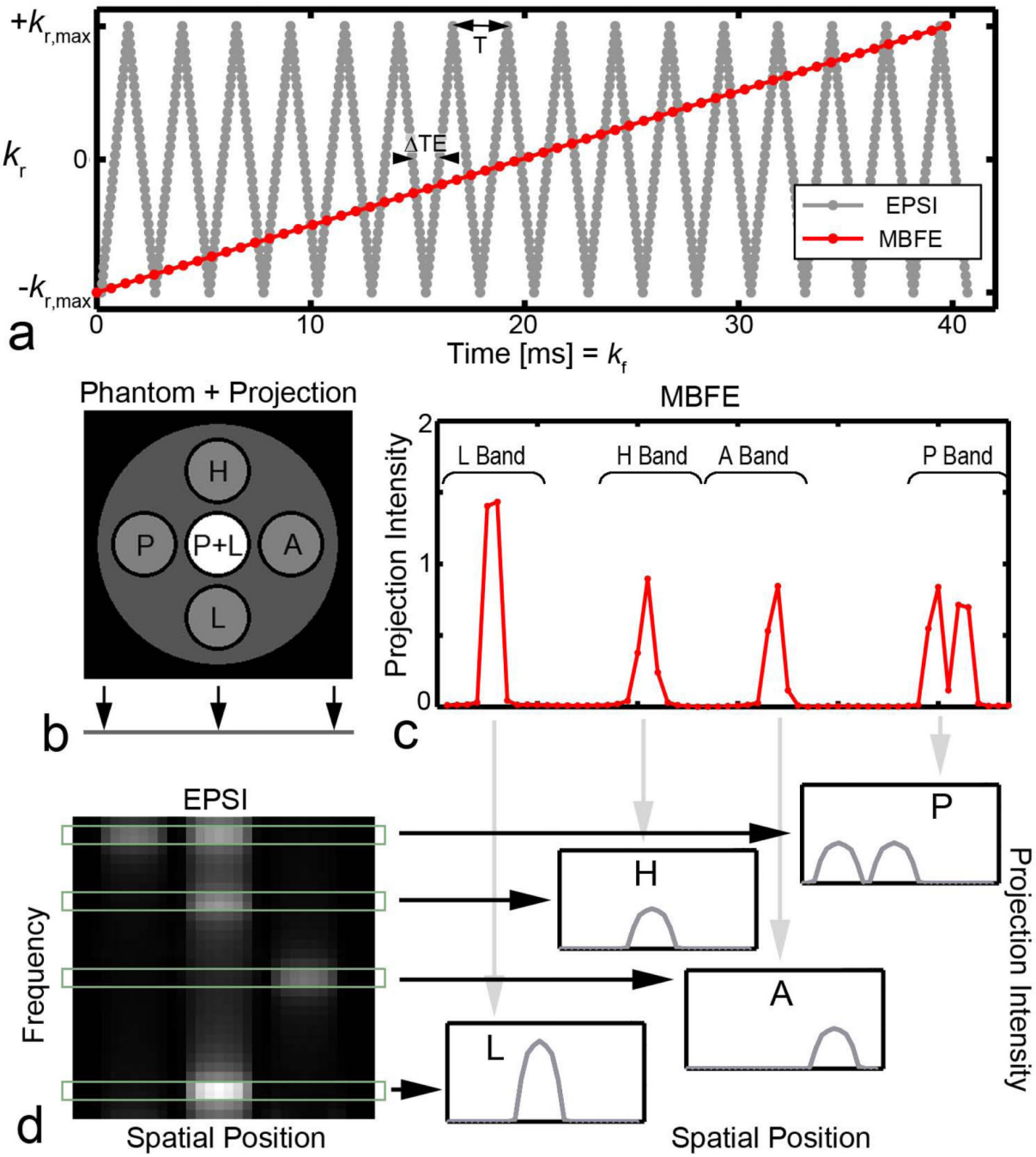

Figure 2.

a. Radial *k*-space trajectories over the acquisition window. A higher gradient switching rate is required for EPSI compared with MBFE. **b**. A multi-compartment phantom containing pyruvate (P at −6.1 ppm), lactate (L at +6.1 ppm), alanine (A at −0.5 ppm), and pyruvate hydrate (H at +2.1 ppm). The axis onto which the object was projected is shown. **c**. Projection data from MBFE version *A* after Fourier transformation, illustrating the location of spectral bands. **d**. After Fourier transformation of corrected EPSI data along k_r and *t*, data may be integrated over spectral peaks to produce high resolution metabolite projections.

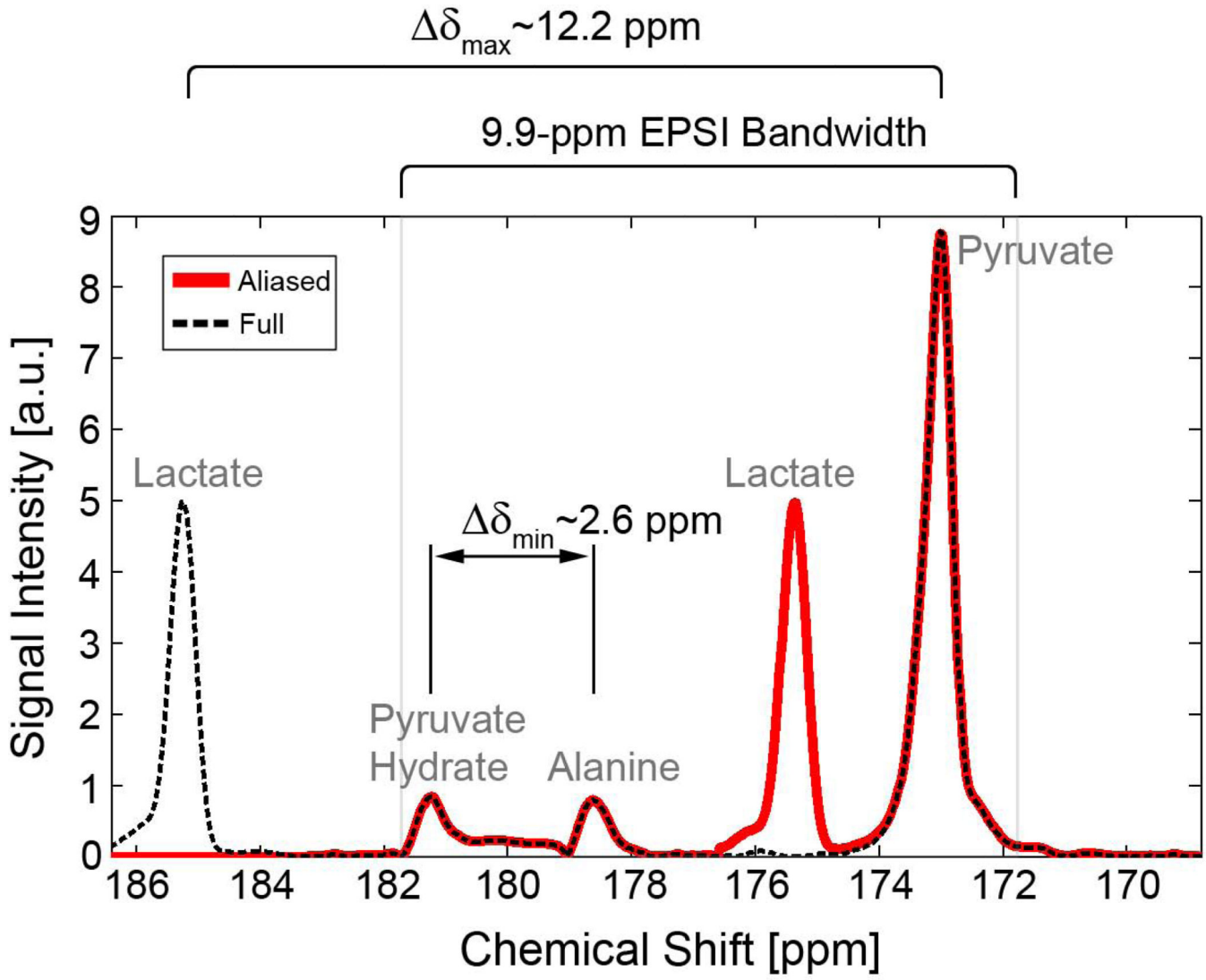

Figure 3.

Slice-localized spectrum illustrating the relationship between spectral peaks and effects of spectral undersampling. A 1.35-ms EPSI echo spacing avoids contamination by spectral overlap from all metabolites and reduces potential contamination from N/2 ghosts of pyruvate affecting the lactate signal. $\Delta\delta_{min}$ and $\Delta\delta_{max}$ are indicated for the full spectrum. If signals from alanine and pyruvate hydrate are low or suppressed, $\Delta\delta_{min} = \Delta\delta_{max}$ and the spatial resolution of MBFE can be significantly improved.

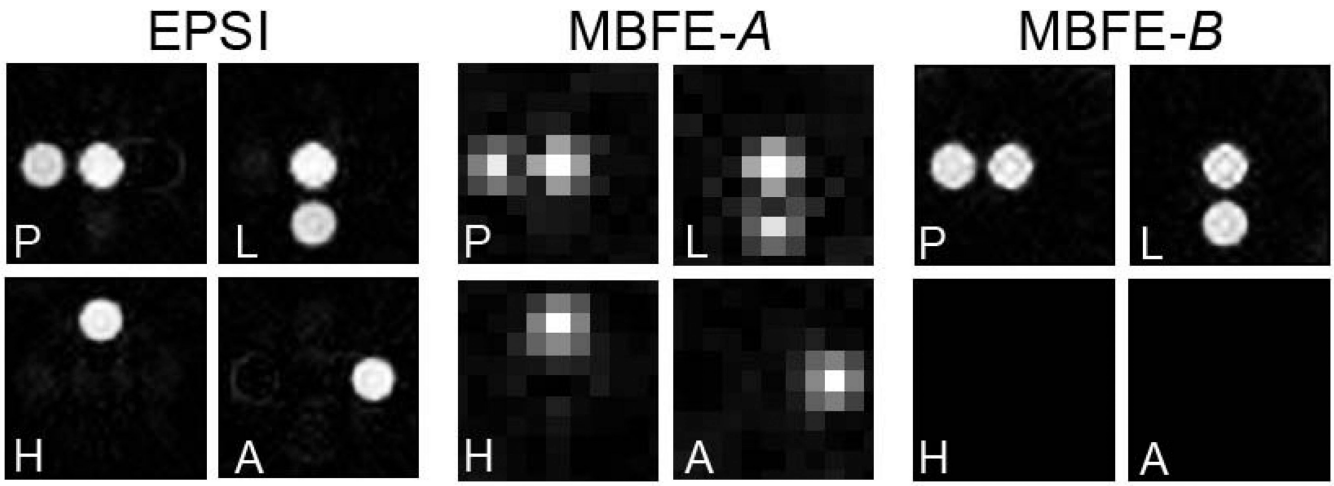

Figure 4.

Reconstructed numerical phantom images from simulated radial EPSI and MBFE ^{13}C-acquisitions. For MBFE, spatial resolution can be significantly increased if pyruvate hydrate and alanine are removed from the phantom (scenario *B*).

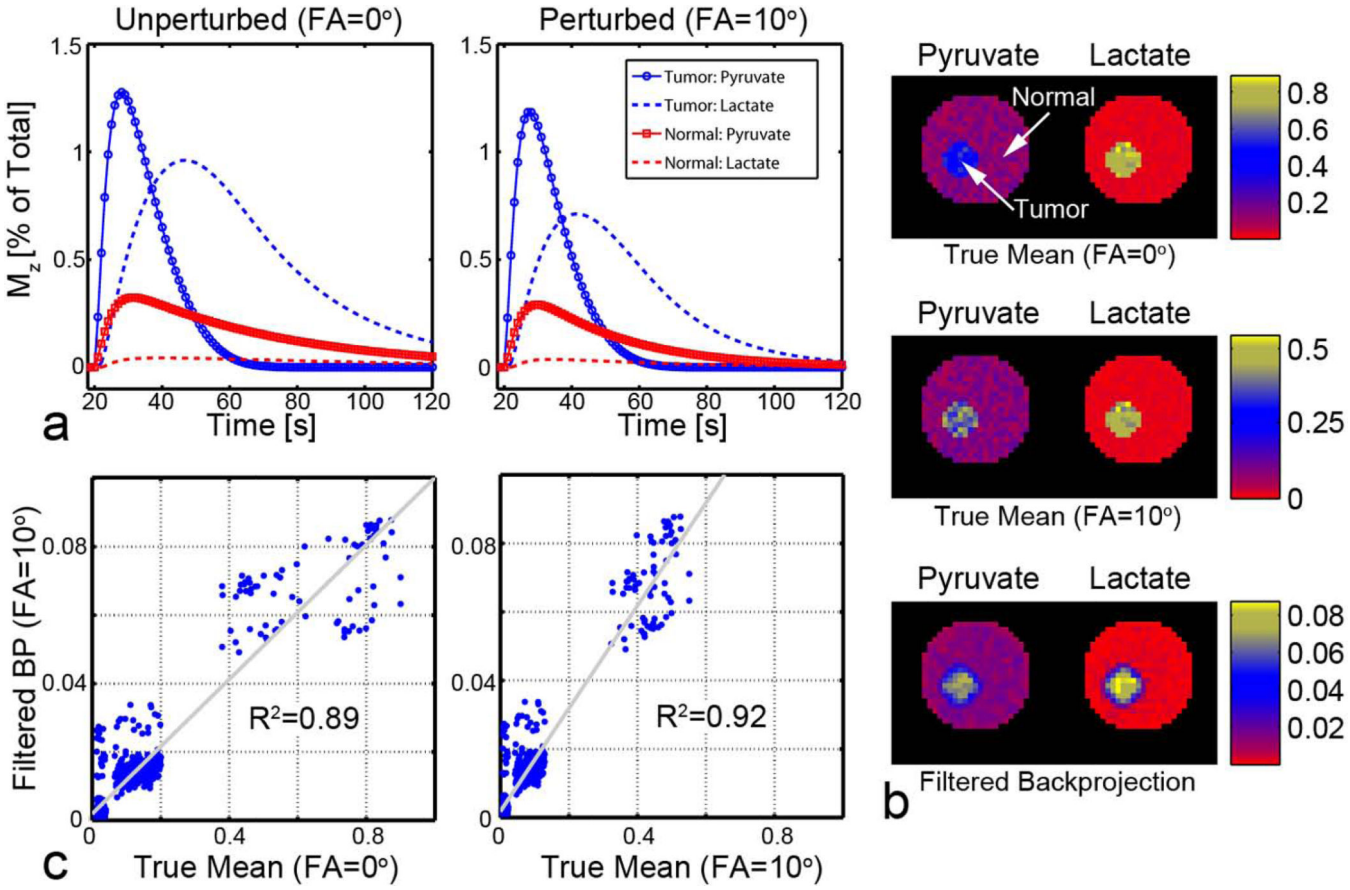

Figure 5.

Cumulative filtered backprojection of data acquired over the observable lifetime of the HP agents. **a**. Representative time-courses of the longitudinal polarization M_z normalized to the total carbon signal, with and without the effect of RF excitation. **b**. The true pixel-by-pixel temporal mean for HP pyruvate and lactate in normal and tumor tissue are visually similar to those achieved with backprojection. **c**. Images generated by simple backprojection correlate well with known pixel-by-pixel temporal averages.

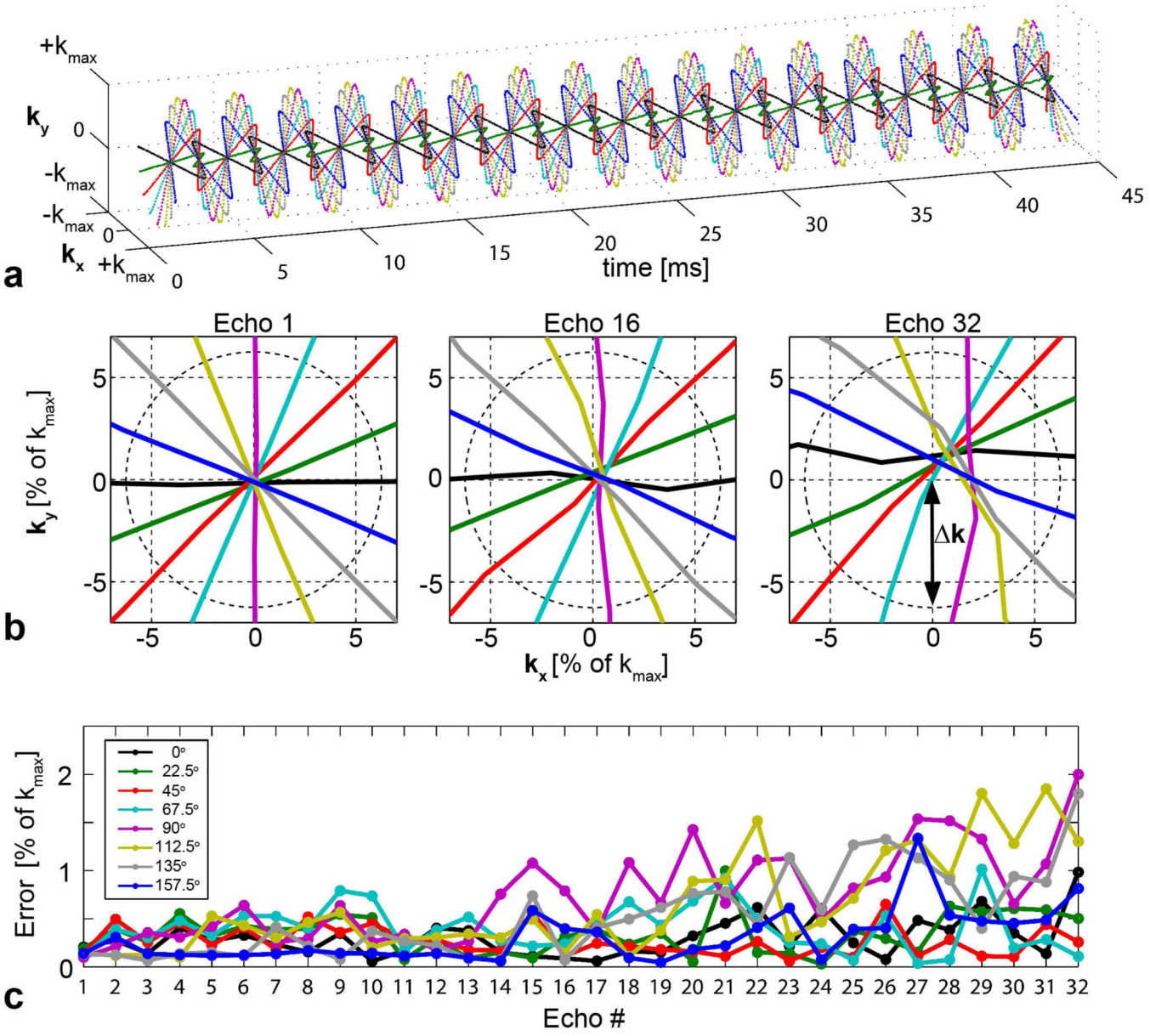

Figure 6.

a. Measured radial EPSI *k*-space trajectories for eight projection angles. **b**. Magnified view of k-space origin for select echoes (1, 16, and 32), showing unit Δk circle reference. Sampling errors are small with respect to Δk. **c**. Distance from k-space trajectory to origin for all echoes. Note that measured trajectories from late echoes contain additional noise due to T_2* relaxation.

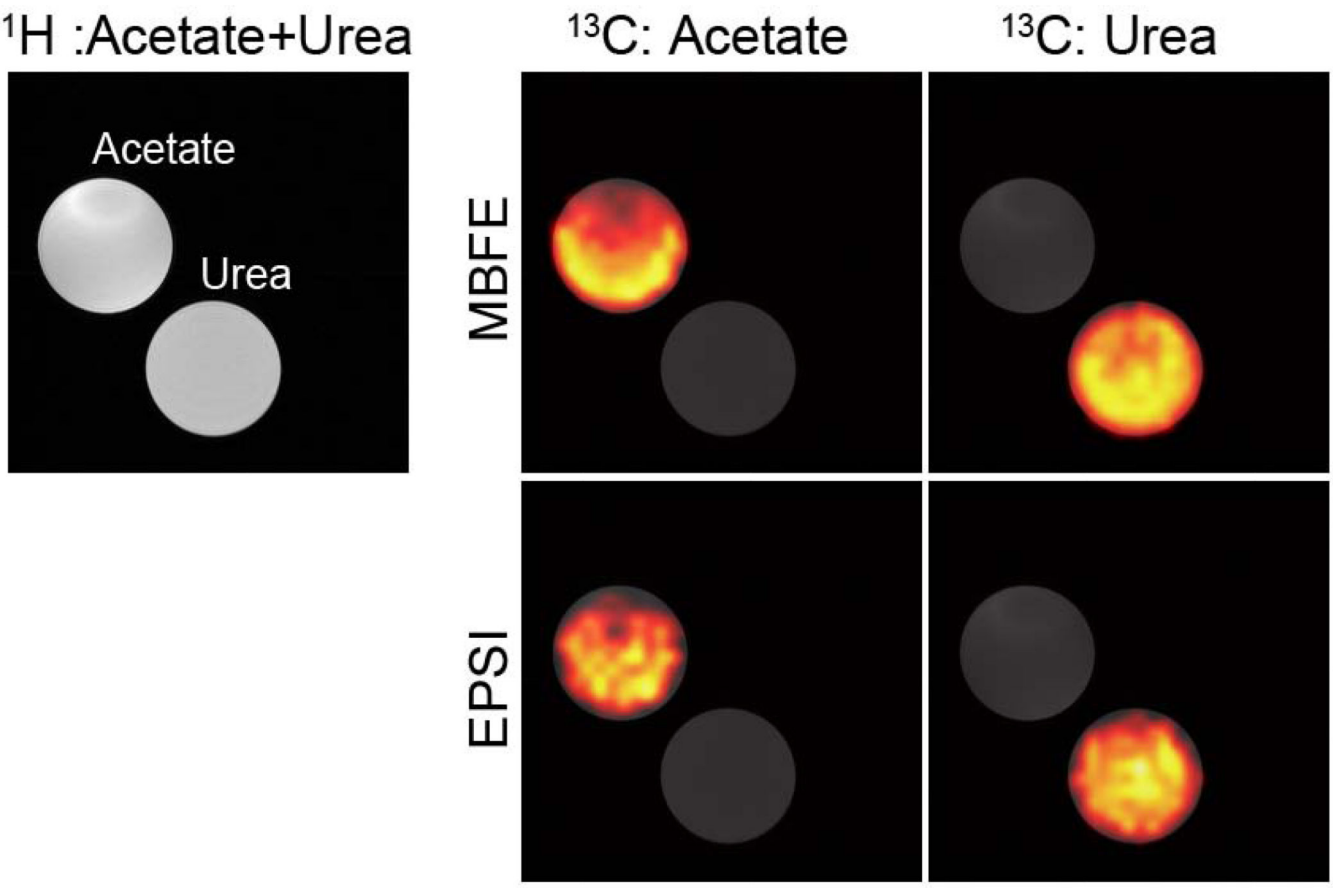

Figure 7.
Radial ^{13}C MBFE and EPSI images of 8-M urea and 3-M acetate phantoms (right) overlaid on the reference ^{1}H images (left).

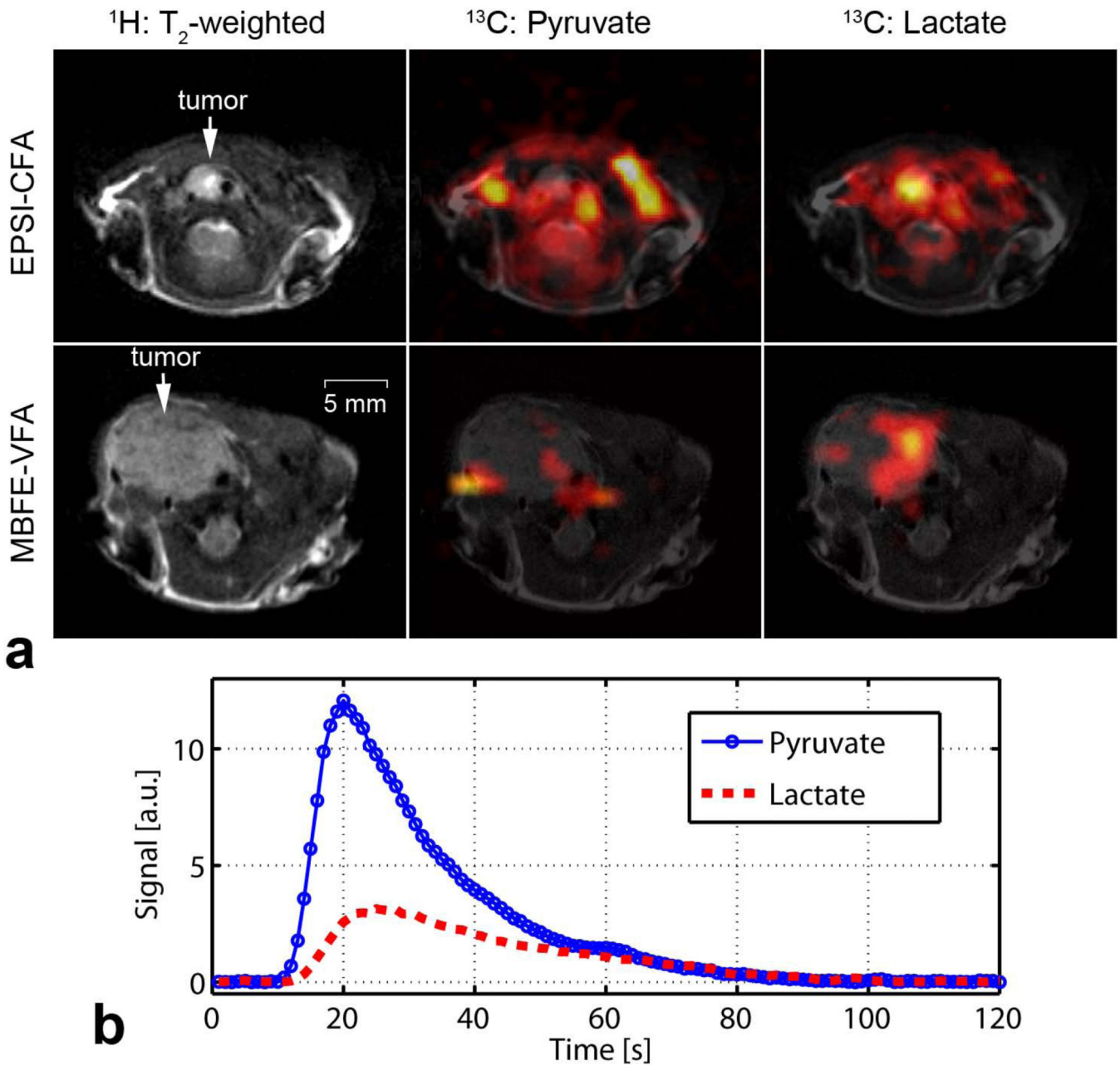

Figure 8.

In vivo imaging of HP pyruvate and lactate in a murine model of anaplastic thyroid cancer. **a**. Results from a 30° constant flip angle (CFA) EPSI acquisition, which sampled throughout the observable duration of the HP agent, are shown on top. Images from a variable flip angle (VFA) MBFE acquisition, which sampled during a 3-s window beginning 25 s after injection, are shown on bottom. Lactate levels appear higher in regions corresponding with tumor compared to normal tissue. Pyruvate appears higher in the image acquired throughout the agent lifetime and near major vessels. ^{13}C images were upsampled by 4× for display. **b**. Dynamic metabolite time courses derived from the radial EPSI acquisition.

Table 1

Selected parameters for radial MBFE and EPSI ^{13}C acquisitions.

	MBFE-*A*	**MBFE-*B***	**EPSI**
$TE_{initial}$ [ms]	26	18	2
$\Delta\delta_{min}$ [ppm]	2.6	12.2	-
N_{read}	57	64	32×32 echoes
N_{bands}	5.7	2	-
points/band	10	32	-
BW_{read} [kHz]	1.12	1.84	24.5
$BW_{spectral}$ [ppm]	14.8	24.4	9.9
$SNR_{relative}$	2.0	1.0	1.3